POLARIZED NEUTRON REFLECTOMETRY AS A UNIQUE TOOL IN MAGNETIZATION REVERSAL STUDIES OF THIN FILMS AND MULTILAYERS

by H. Fritzsche, Z. Yamani, R. Cowley and R.C.C. Ward

Typically, the magnetization reversal behavior of thin magnetic films and multilayers is studied with magnetometers (*e.g.* a vibrating sample magnetometer or a superconducting quantum interference device) or with the magneto-optical Kerr effect. In this article we show how Polarized Neutron Reflectometry (PNR) can be used as a tool to measure hysteresis loops and to study the magnetization reversal behavior of magnetic multilayers in more detail. We will discuss the instrumental setup needed to perform PNR experiments along with the theoretical background of this technique. In contrast to conventional magnetometers capable of measuring only the average magnetization of a multilayer, PNR is able to determine the magnetization profile and can distinguish between the magnetizations of different magnetic layers in a multilayer. This feature of PNR being element-specific, will be demonstrated with the magnetization reversal study of a (6 nm $ErFe_2$ / 6 nm $DyFe_2$) multilayer, where we were able to follow the magnetization reversal of the $ErFe_2$ and $DyFe_2$ magnetizations independently.

In this article we show how Polarized Neutron Reflectometry (PNR) can be used as a tool to measure hysteresis loops and to study the magnetization reversal behavior of magnetic multilayers in more detail.

INTRODUCTION

During the last two decades Polarized Neutron Reflectometry (PNR) has become a very powerful and popular technique in the study of magnetic properties of thin films and multilayers. PNR has drawn a lot of attention of the scientific community due to the study of the oscillatory exchange coupling in Fe/Cr [1,2], Co/Cu [3] or Fe/Nb [4,5] multilayers. PNR is the method of choice to prove the antiferromagnetic coupling of the magnetizations of ferromagnetic layers (*e.g.* Fe) separated by non-ferromagnetic layers (*e.g.* Cr) because the antiparallel alignment of the magnetic layers gives rise to an additional peak in the reflectivity curve. Even more complicated structures such as a non-collinear 50° coupling [6] or a helical magnetic structure [7] can be determined by PNR. Another area where PNR has been applied very successfully is the determination of the absolute magnetic moment of ultrathin Fe and Co films [8,9,10] to study surface and size effects. Here, the big advantage of PNR is that the substrate does not contribute to the magnetic signal unlike in conventional magnetometry measurements where the diamagnetic signal of the substrate dominates over the tiny magnetic signal originating from the sample.

Only recently PNR was used to study the magnetization reversal of thin films [11,12]. Thin magnetic films are used as magnetic field sensors and therefore it is very important to understand the magnetization reversal process and to distinguish between a domain wall movement and a rotation process because generally magnetic domains give rise to electrical noise and reduce the performance of a sensor [13]. Exchange-bias systems consisting of a ferromagnet in direct contact with an antiferromagnet represent an essential component of thin-film systems used as sensors. PNR shed light on the asymmetric magnetization reversal of these exchange-biased multilayers [11,14,15,16,17]. For the Co/CoO system PNR experiments revealed a rotation process of small domains for increasing fields and a domain-wall motion for decreasing fields during the first cycle of a hysteresis loop.

In this article we provide an introduction to the theoretical description of PNR along with some model simulations of reflectivity curves followed by a description of the essential components needed to set up a polarized neutron reflectometry experiment. How PNR can yield layer-sensitive information for a magnetization reversal of a multilayer consisting of two different ferromagnetic layers is shown for the case of a (6 nm $ErFe_2$ / 6 nm $DyFe_2$) multilayer. These types of multilayers are of technological interest because they have potential applications for sensors and magnetic read heads.

THEORETICAL DESCRIPTION OF PNR AND MODEL SIMULATIONS

The scattering geometry of a typical reflectometry experiment is shown in Fig. 1. The neutron beam hits the surface at an angle θ and the reflected intensity is simply measured as a function of θ, which is typically in the range between 0 and 2°. The interfaces of the samples are arranged perpendicular to the scattering vector

$$|\vec{q}| = |\vec{k}_f - \vec{k}_i| = \frac{4\pi}{\lambda}\sin(\theta) \qquad (1)$$

with $\vec{k}_i$ and $\vec{k}_f$ being the incoming and outgoing neutron wave vector and λ the neutron wavelength. The neutron spins are

H. Fritzsche[a] <Helmut.Fritzsche@nrc-cnrc.gc.ca>, Z. Yamani[a], R. Cowley[b], R.C.C. Ward[b]; [a]National Research Council Canada, CNBC, Chalk River Labs, Chalk River, ON, K0J 1J0, Canada; [b]Oxford Physics, Clarendon Laboratory, Parks Road, Oxford OX1 3PU, UK

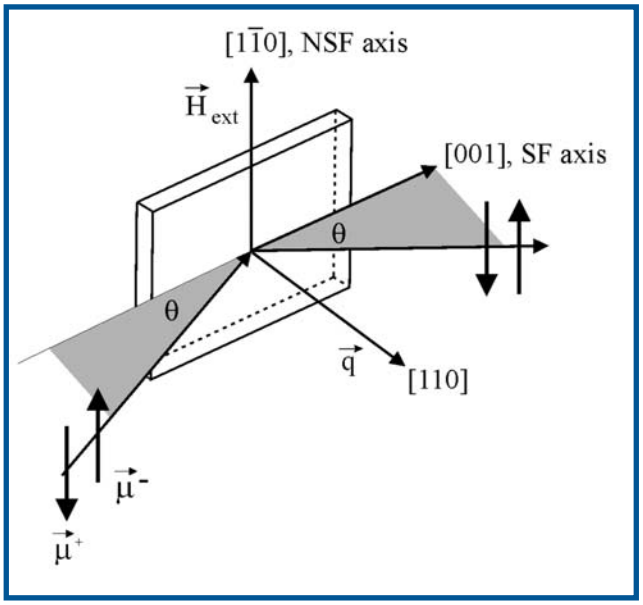

Fig. 1 **Scattering geometry for a neutron reflectometry experiment with the scattering angle θ, scattering vector $\vec{q}$, the external magnetic field $\vec{H}_{ext}$, and the magnetic moment of the spin-up neutrons ($\vec{\mu}^+$) and spin-down neutrons ($\vec{\mu}^-$). The spin-flip (SF) axis as well as the non-spin flip (NSF) axis is indicated along with the crystallographic orientation used for the experiments on the ($ErFe_2$/$DyFe_2$) multilayer.**

oriented either parallel to the external field (spin-up neutrons) or antiparallel (spin-down neutrons) to the external field which is in the film plane (see Fig. 1). The interaction with the film is reduced to a one-dimensional problem, which can be described for grazing incidences with an effective potential that is a sum of a nuclear and a magnetic component (the Zeeman interaction). For the case that the sample's magnetization is parallel to the external field this potential V_j in layer j is given by:

$$V_j = \frac{2\pi\hbar^2}{m} N_j b_j^{nuc} - \vec{\mu}\cdot\vec{B}_j \qquad (2)$$

where m and $\vec{\mu}$ denote the neutron mass and magnetic moment and N_j, b_j^{nuc}, and $\vec{B}_j$ denote the atomic density, coherent nuclear scattering length, and magnetic induction in layer j. The first term in Eq. (2) results from the interaction of the neutron with the nucleus, while the second term results from the interaction of the neutron with the magnetization of the sample. The product $N_j b_j^{nuc}$ is known as the nuclear scattering length density (SLD). The magnetic part of the potential depends on the orientation of the magnetic induction with respect to the magnetic moment of the neutrons. It is important to note that we are not sensitive to a perpendicular magnetization component in the PNR setup sketched in Fig. 1. The magnetic contribution to the potential can also be expressed in terms of a magnetic SLD $N_j b_j^{mag}$, which makes it convenient to discuss the sample's properties in terms of SLDs. According to Eq. 2 the potential V^+ for spin up and V^- for spin down neutrons is different and they can be expressed in terms of a magnetic SLD as follows:

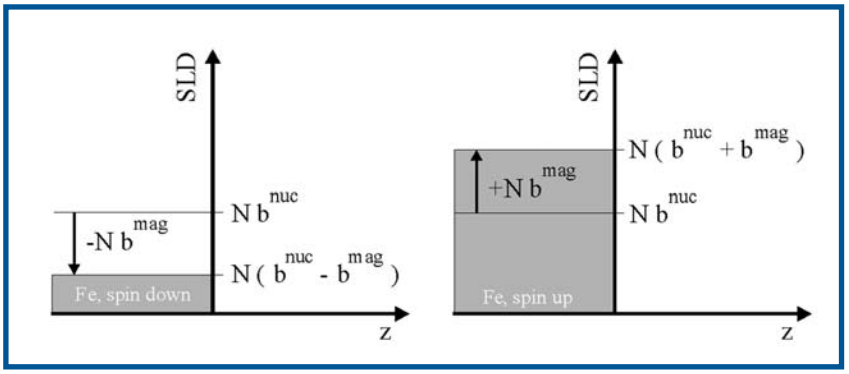

Fig.2 **The scattering length density (SLD) for spin-down neutrons (left) and spin-up neutrons (right) for the case of bulk Fe. The SLD is composed of a nuclear and a magnetic part.**

$$V_j^{\pm} = \frac{2\pi\hbar^2}{m}\left(N_j b_j^{nuc} \pm N_j b_j^{mag}\right) \qquad (3).$$

PNR is very sensitive to magnetic structures because the nuclear and magnetic SLDs are of the same order of magnitude. The nuclear SLD depends on the elements and their isotopes in the sample [18,19]. A diagram of the SLD and the simulated reflectivity curves for the case of bulk Fe saturated along the external field (Nb^{nuc} = 801.9 μm^{-2} and Nb^{mag} = 498.5 μm^{-2}) is shown in Fig. 2 and Fig. 3, respectively. The solid line in Fig. 3 denotes R^+, the reflectivity of spin-up neutrons, the dashed line is R^-, the reflectivity of down neutrons. The reflectivity of the sample can be calculated by solving the Schrödinger equation using the above mentioned potential. The simulations presented here were calculated with software based on the Parratt formalism [20]. The critical edge q_c up to which total reflectivity (R=1) is observed is different for spin-up and spin-down neutrons and depends on the SLD in the following way:

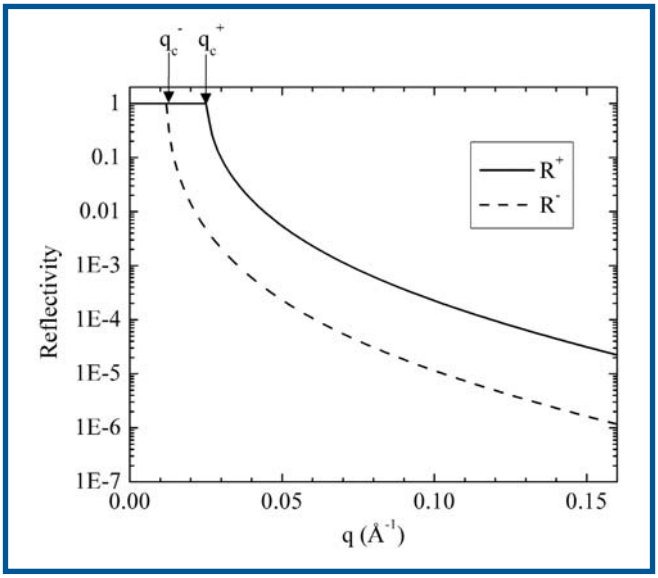

Fig. 3 **Simulated reflectivity curves of a bulk Fe sample for spin-up neutrons (R^+, solid line) and spin-down neutrons (R^-, dashed line).**

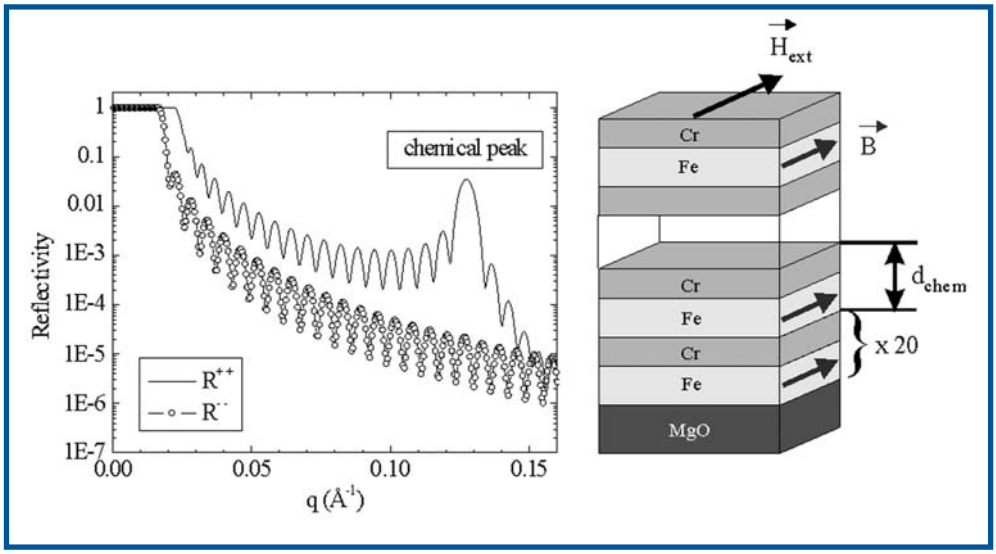

Fig. 4 Simulated reflectivity curves and magnetic structure of a ferromagnetically aligned (4 nm Fe / 1 nm Cr)$_{20}$ multilayer in an external magnetic field H$_{ext}$. Clearly observable is the chemical peak at q = 0.127 Å^{-1} due to the chemical modulation of the multilayer.

$$q_c^{\pm} = \sqrt{16\pi N(b^{nuc} \pm b^{mag})} \qquad (4).$$

The simulated reflectivity curves of a ferromagnetically aligned (4 nm Fe / 1 nm Cr)$_{20}$ multilayer along with the magnetic structure of the multilayer is depicted in Fig. 4. In this case, the chemical period d_{chem} is identical to the magnetic period and leads to a Bragg peak at $q = 2\pi/d_{chem}$. Analogous to the case of bulk Fe, the critical scattering vector q_c^+ for spin-up neutrons is larger than the critical scattering vector q_c^- for spin-down neutrons. For the case of an antiferromagnetic alignment of the Fe layers, as shown in Fig. 5, the magnetic period d_{AF} is now twice the chemical period and leads to an additional peak at $q = 2\pi/d_{AF}$. The existence of this additional peak shows immediately that the ferromagnetic layers are oriented antiparallel with respect to each other. As the total magnetization of the multilayer is zero, the critical scattering vector for spin-up and spin-down neutrons are identical.

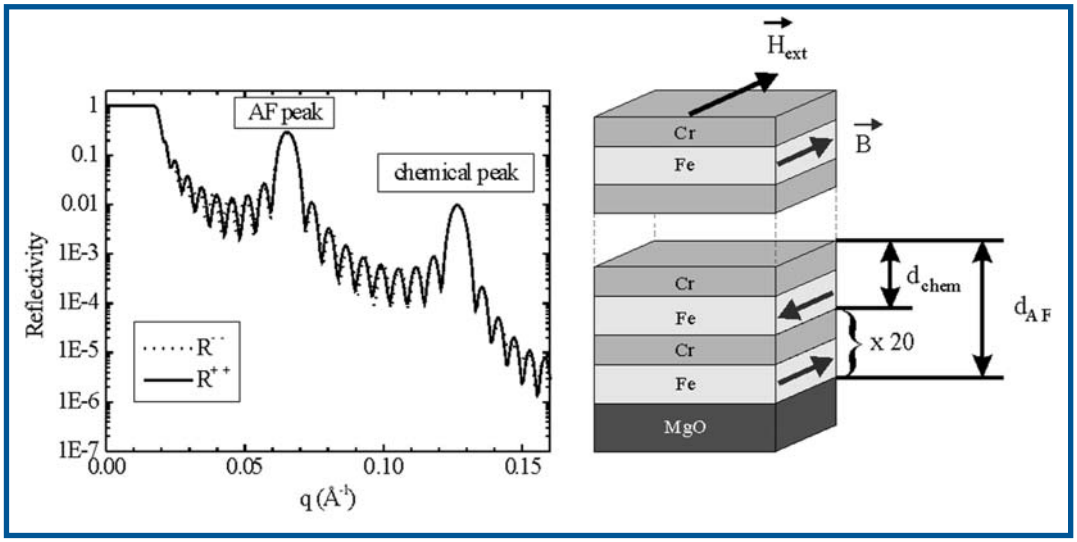

Fig. 5 Simulated reflectivity curves and magnetic structure of an antiferromagnetically aligned (4 nm Fe / 1 nm Cr)$_{20}$ multilayer with its magnetizations collinear with the external field. Clearly observable is the chemical peak at q = 0.127 Å^{-1} due to the chemical modulation of the multilayer and the AF peak at q = 0.065 Å^{-1} due to the magnetic modulation of the multilayer.

So far we only discussed cases where the magnetization is collinear with the external field. The big advantage of PNR is that it is also sensitive to in-plane magnetization components perpendicular to an external field. These perpendicular components (parallel to the [001] direction in Fig. 1) give rise to a so-called spin-flip process, *i.e.* an incoming spin-down neutron will be reflected as a spin-up neutron and vice-versa. The spin-flip scattering is proportional to $|\vec{\mu}x\vec{B}|$ and is maximum if the whole magnetization is perpendicular to the external field or the neutron spin, respectively. As shown in Fig. 6, the antiferromagnetic structure of a Fe/Cr multilayer can be observed as a peak in the spin-flip reflectivities R^{-+} and R^{+-} if the magnetization of the Fe layers is perpendicular to the external field. At the same time no antiferromagnetic peak can be observed in the non-spin flip reflectivities R^{++} and R^{--}. The two superscripts of the reflectivities denote the spin state of the neutrons before and after reflection from the sample. This sensitivity of PNR to magnetization components parallel and perpendicular to the external field has been exploited, *e.g.* to study the spin-flop transition in an antiferromagnetically coupled Fe/Cr multilayer [21]. At low fields the magnetization is collinear with the external field. When increasing the external field the whole magnetic structure rotates at a certain field value from a collinear alignment like in Fig. 5 to a perpendicular arrangement as shown in Fig. 6. So, where conventional magnetometers would simply measure an averaged zero magnetization, PNR can determine the magnetic structure of the magnetic multilayer in more detail and even distinguish between the two types of antiferromagnetic alignment shown in Figs. 5 and 6. More detailed information on the theoretical description of PNR and fitting algorithms can be found elsewhere [22,23,24].

INSTRUMENTAL SETUP

The C5 triple axis spectrometer at the neutron reactor NRU in Chalk River was used to perform the neutron reflectometry experiments described in the next section. The (111) reflection of a Cu_2MnAl

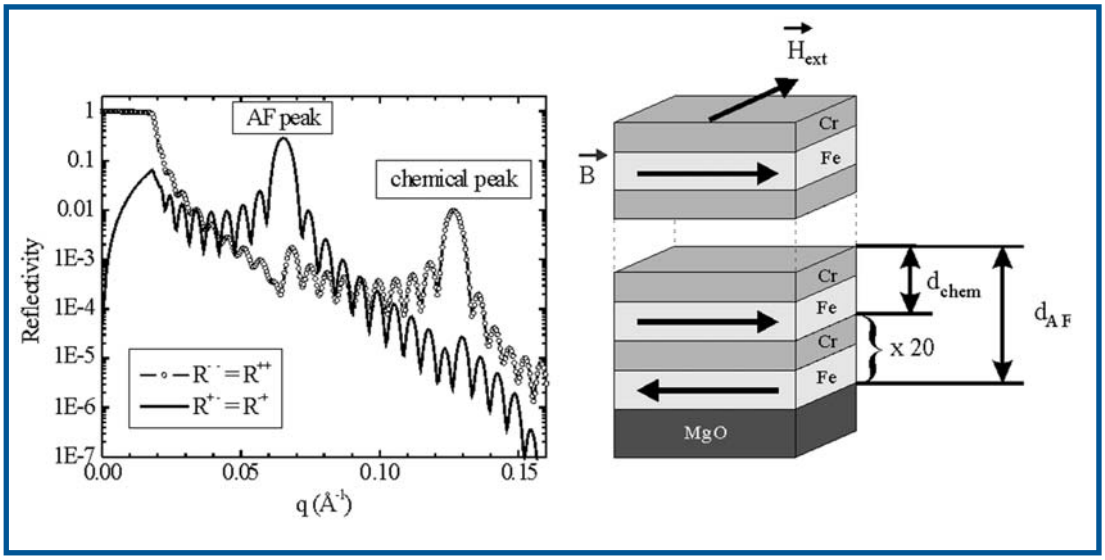

Fig. 6 **Simulated reflectivity curves and magnetic structure of an antiferromagnetically aligned (4 nm Fe / 1 nm Cr)$_{20}$ multilayer with its magnetizations perpendicular to the external field. Clearly observable is the chemical peak at q = 0.127 Å^{-1} in the non-spinflip reflectivities R^{--} and R^{++} due to the chemical modulation of the multilayer and the AF peak at q = 0.065 Å^{-1} in the spin-flip reflectivities R^{-+} and R^{+-} due to the magnetic modulation of the multilayer.**

Heusler crystal is used to polarize and analyze the neutrons' spin state at a wavelength of λ=0.237 nm in combination with a pyrolitic graphite (PG) filter which reduces the higher order contributions of a monochromator (λ/2, λ/3, etc.) [25] by a factor of about 1000. The distances from the monochromator to the first slit, first slit to second slit, and second slit to sample were 0.16 m, 1.44 m, and 0.18 m, respectively. A sketch of the setup is displayed in Fig. 7. The components needed are a monochromator (M) and analyzer crystal (A), slit systems (S1, S2, S3, and S4), spin flippers (SF1 and SF2), a PG filter (F), a sample, and a detector (D). The slits S1 and S2 define the collimation of the beam, whereas the slits 3 and 4 reduce the background. The detector is a 5 bar ^{3}He gas detector.

The maximum achievable polarization by using the (111) Bragg reflection of a Cu_2MnAl Heusler crystal can be easily calculated from the different structure factor for up neutrons and down neutrons. The intensity I^+ and I^- for up and down neutrons, respectively, is simply, ignoring element-specific Debeye-Waller factors:

$$I^+ \sim I_0 \times (b_{nuc,\,Mn} - b_{nuc,\,Al} + b_{mag,\,Mn})^2 \sim I_0 \times 2.09 \qquad (5)$$

$$I^- \sim I_0 \times (b_{nuc,\,Mn} - b_{nuc,\,Al} - b_{mag,\,Mn})^2 \sim I_0 \times 249.7 \qquad (6)$$

where $b_{nuc,\,Mn}$ = -3.73 fm denotes the nuclear scattering length of Mn, $b_{nuc,\,Al}$ = 3.449 fm denotes the nuclear scattering length of Al, and $b_{mag,\,Mn}$ = 3.2×2.695 fm denotes the magnetic scattering length of Mn with 3.2 μ_B per Mn atom at room temperature. The neutron beam polarization P is defined as:

$$P = \frac{I^- - I^+}{I^- + I^+} \qquad (7)$$

and in the case of a perfect Heusler crystal the maximum achievable polarization is 98.3%.

As the polarizer delivers only spin-down neutrons, we need a device called "spin flipper" (SF1) located after the polarizer to convert spin-down neutrons into spin-up neutrons in order to be able to measure the reflectivity curve of spin-up neutrons as well. Another spin flipper is needed in front of the analyzer (SF2) to determine the spin state of the reflected neutrons. At reactor sources Mezei-type spin flippers [26] are commonly used. They consist of two solenoids with rectangular cross section. One solenoid flips the neutron's spin and the other one compensates the stray fields. The field produced by the compensation coil is collinear with the guide field, whereas the flip field is perpendicular to the guide field. Therefore, the neutron's spin precesses in the flip field and one has to adjust the magnetic field produced by this solenoid by tuning the current through the flipper coil in order to achieve exactly a π rotation when the neutrons pass through the magnetic field region. A magnetic guide field of at least a few Gauss is always needed along the neutron path in order to preserve the spin polarization.

The polarization of the beam can be determined by measuring the flipping ratio F, *i.e.* $F^- = I^{--}/I^{-+}$ for spin-down neutrons or $F^+ = I^{++}/I^{+-}$ for spin-up neutrons, respectively. The polarization of the neutron beam can be deduced via:

$$P = \sqrt{\frac{I^{--} - I^{-+}}{I^{--} + I^{-+}}} = \sqrt{\frac{I^{--}(1 - 1/F)}{I^{--}(1 + 1/F)}} = \sqrt{\frac{F-1}{F+1}} \qquad (8).$$

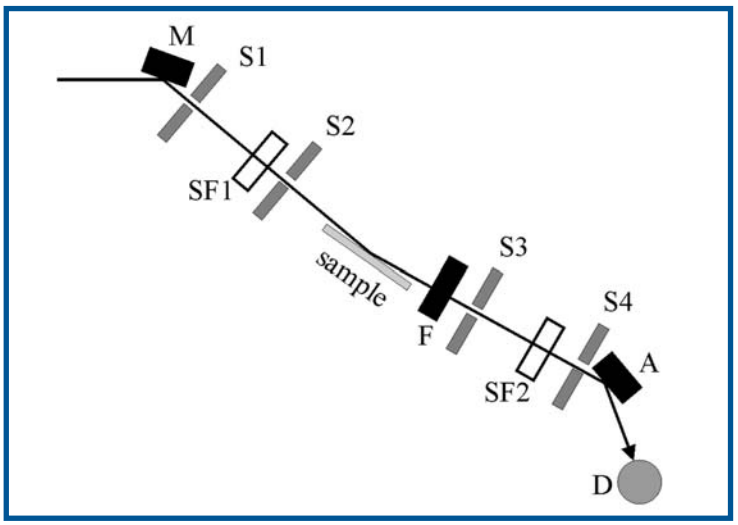

Fig.7 **Neutron reflectometry set-up using a polarizing monochromator (M) and analyzer crystal (A), slit systems (S1, S2, S3, and S4), spin flippers (SF1 and SF2), a PG filter (F), and a detector (D).**

The square root is used here because the neutrons are reflected twice, from the monochromator and the analyzer, using for both the same type of crystal, in our case a Heusler crystal. In our setup we typically achieve flipping ratios higher than 25 corresponding to a polarization of about 96%.

The experiments on the (6 nm $ErFe_2$ / 6 nm $DyFe_2$)$_{40}$ multilayers were carried out in a magnetic field of up to 6 T using a cryomagnet because the rare earth / iron alloys are well-known for their huge magnetic anisotropies and therefore, a large external magnetic field is needed to saturate the sample's magnetization along certain crystallographic directions. The additional measures needed to maintain the neutrons' polarization in the presence of huge magnetic stray fields of a cryomagnet is described elsewhere [27].

MAGNETIZATION REVERSAL OF A (6 nm $ErFe_2$ / 6 nm $DyFe_2$)$_{40}$ MULTILAYER

During the last decade there has been an increasing interest in thin films and multilayers composed of rare earth materials because they have many potential technical applications as sensors and magnetic read heads. In the ($ErFe_2$ / $DyFe_2$) multilayer system both the $DyFe_2$ and the $ErFe_2$ layers are hard magnets but with different easy axes in the bulk samples. The term "easy axis" describes the direction in which the magnetization prefers to lie without an external field. Bulk $DyFe_2$ has the crystallographic <100> directions as easy axes, whereas bulk $ErFe_2$ has its easy axes along the <111> directions. This can lead to very complex magnetic structures when considering that additional anisotropies such as interface, shape, and strain anisotropy, are present in these thin magnetic films [28,29,30]. On top of that there exists an exchange interaction between the Fe atoms of adjacent layers that strongly favors a parallel alignment of the magnetizations.

The magnetic structure of both the $ErFe_2$ and $DyFe_2$ is called ferrimagnetic because the magnetic moment of the Fe atoms is antiparallel and unequal to the magnetic moment produced by the rare earth atoms Dy and Er. Below room temperature the magnetic moment produced by the rare earths is larger, and therefore the net magnetization of the layers points always along the direction of the rare earth magnetization.

The sample was grown using the molecular beam epitaxy facility in the Clarendon Laboratory, Oxford. Sapphire substrates with a $(11\bar{2}0)$ orientation were cleaned and 100 nm niobium was deposited as a chemical buffer layer, followed by a 2 nm iron seed to improve the crystal growth [31]. The multilayer was then grown by co-deposition of the elementary fluxes with a layer thickness of 6 nm for both layers, repeating the ($ErFe_2$ / $DyFe_2$) sequence 40 times. Finally the multilayer was covered with a 10 nm thick yttrium layer as a protection against oxidation. Both layers, $DyFe_2$ and $ErFe_2$, had a (110) surface orientation.

In Fig. 8 a series of reflectivity curves are shown during a magnetization reversal cycle at a temperature of T = 100 K. Prior to the measurements the sample has been saturated in a field of –6 T with the field along the in-plane $[1\bar{1}0]$ direction. The sample's orientation with respect to the magnetic field and the neutron spins is depicted in Fig. 1. After having reached the negative saturation the magnetic field was ramped down to zero and reversed to positive values. The shown reflectivity curves were recorded at a field of 0.4 T (top panel), 1 T (middle), and 6 T (bottom). Only the non-spin flip reflectivities for down neutrons (R^{--}, open circles) and up-neutrons (R^{++}, closed circles) are shown, the measured spin-flip reflectivities R^{-+} and R^{+-} were zero within errors. In the top panel of Fig. 8 it can be clearly seen that the critical scattering vector up to which total reflectivity occurs, is larger for R^{--} than for R^{++}. That proves that the magnetization in a positive field of 0.4 T is still reversed, *i.e.* antiparallel to the applied field. In positive saturation, as shown in the bottom panel, the critical scattering vector for R^{--} is much smaller than that for R^{++}. The coercive field is about 1 T as can be seen in the middle panel because the reflectivity curves for spin-up and spin-down neutrons are very similar, especially the critical scattering vectors for both cases are very close to

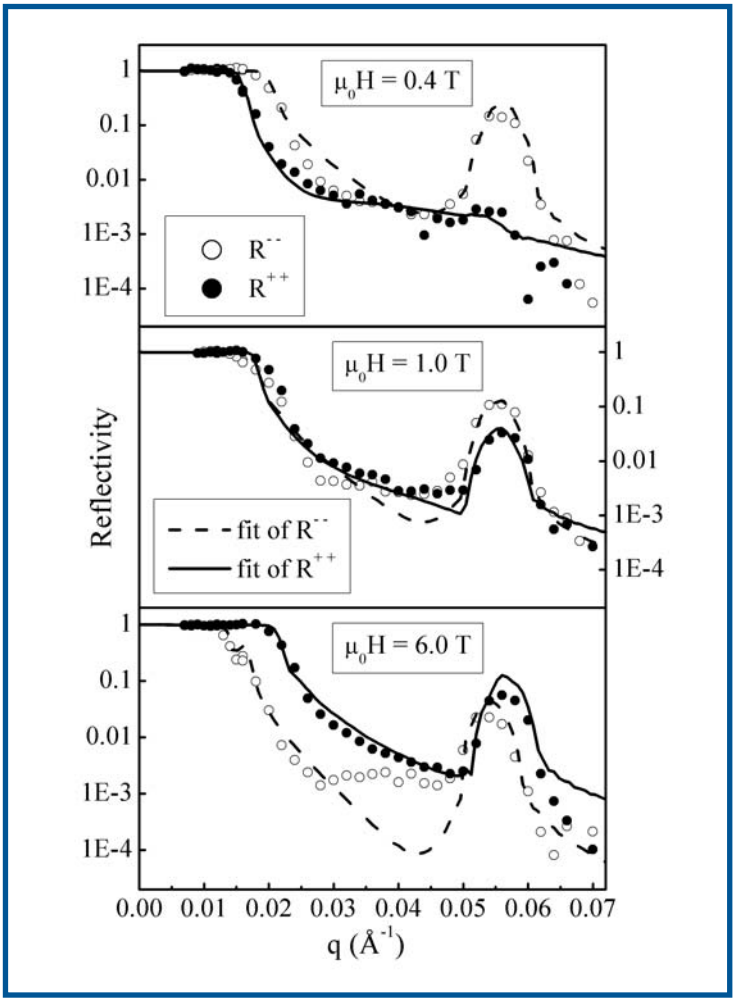

Fig. 8 Measured neutron reflectivities R^{++} (solid circles) and R^{--} (open circles) of a (6 nm $ErFe_2$ / 6 nm $DyFe_2$)$_{40}$ multilayer along with the fits (solid and dashed line, respectively) at a temperature T=100 K, in an external magnetic field of 0.4 T (top panel), 1 T (middle panel), and 6 T (bottom panel). Prior to the measurements, the magnetization of the sample was reversed in a field of –6 T, the field was always applied along the [1 1 0] in-plane direction.

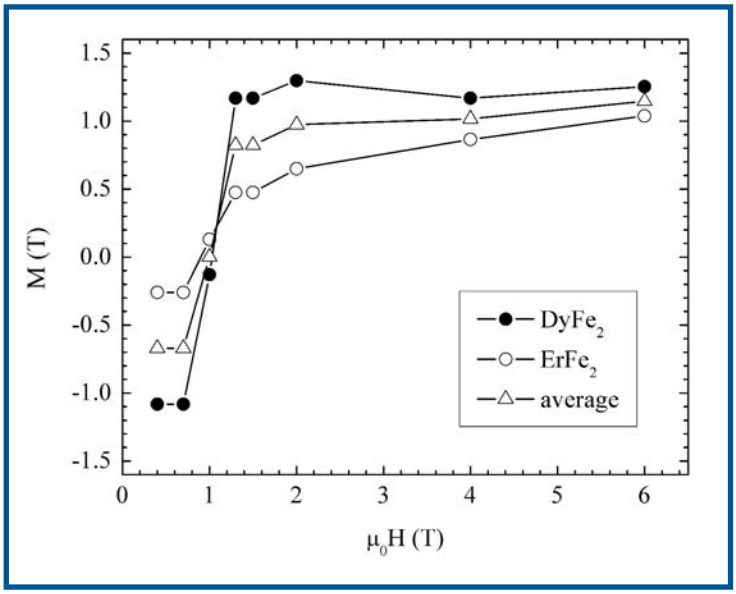

Fig. 9 Magnetization component along the external field of the $DyFe_2$ layers (solid circles), $ErFe_2$ layers (open circles), and the average magnetization of the (6 nm $ErFe_2$ / 6 nm $DyFe_2$)$_{40}$ multilayer (triangles) as a function of the external field at a temperature of 100 K. Prior to the measurements, the magnetization of the sample was reversed in a field of –6 T, the field was always applied along the [1 $\bar{1}$ 0] in-plane direction.

each other. For a completely demagnetized sample the spin-up reflectivity would equal the spin-down reflectivity. An important observation was that no increased spin-flip signal was observed at 1 T. That means that there is no homogeneous in-plane rotation of the magnetization. The magnetization must be reversed either by domain wall movement or a magnetization rotation perpendicular to the sample's surface because in PNR we are not sensitive to magnetization components perpendicular to the sample's surface.

The reflectivity curves shown in Fig. 8 were fitted using the Parratt formalism [20]. The solid line represents the fit to the spin-up reflectivity, whereas the dashed line represents the fit to the spin-down reflectivity. From the fit data we can infer the magnetization component of the $DyFe_2$ and $ErFe_2$ layer parallel to the external field independently. The values are shown in Fig. 9 with the closed circles representing the magnetization component of the $DyFe_2$ layers and the open circles representing the magnetization component of the $ErFe_2$ layers. The average value, as it would be measured by classical magnetometry is displayed as triangles. It can be clearly seen that the behavior of the two magnetizations is different. The magnetization curve of the $DyFe_2$ represents an easy axis loop with a very fast switching from negative to positive saturation. In contrast, the $ErFe_2$ magnetization curve represents a hard axis loop where the magnetization rotates continuously towards the direction of the magnetic field. This nicely shows the capability of PNR to be element-specific.

This property of PNR to be element-specific is underlined in Fig. 10 where simulated reflectivity curves are shown for three different cases of a magnetic structure giving a zero signal in a classical magnetometer. In the top panel the magnetization of the $DyFe_2$ (M_{DyFe2} = -0.13 T) is antiparallel to the external field, whereas the magnetization of the $ErFe_2$ layer (M_{ErFe2} = 0.13 T) is parallel to the external field. This corresponds to the magnetic structure at the coercive field as deduced from our PNR data at a magnetic field of 1 T (Fig. 8, middle panel). As can be seen in the middle panel of Fig. 10, where the directions of both magnetizations are swapped, the intensity ratio of R^{++} to R^{--} at the Bragg peak position is swapped as well. So, it is easy in a PNR experiment to distinguish between these two cases and it shows that the PNR data in Fig. 8 (middle panel) could not have been fitted with a magnetic structure where the directions of both layer magnetizations are reversed. For comparison, the case for zero magnetization, where $R^{++} = R^{--}$, is displayed in Fig. 10 (bottom panel).

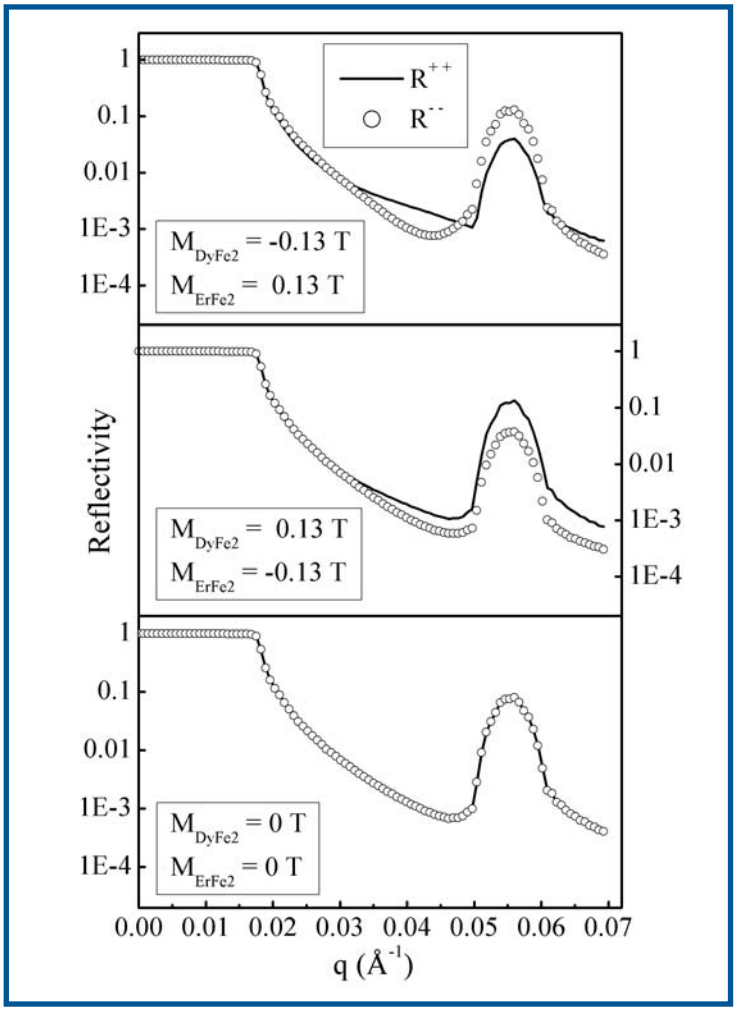

Fig. 10 Simulation of R^{++} and R^{--} for different magnetic structures in a (6 nm $ErFe_2$ / 6 nm $DyFe_2$)$_{40}$ multilayer: in the top panel for the case where the magnetization of the $DyFe_2$ layers is antiparallel to the external field, the magnetization of the $ErFe_2$ layers parallel to the external field, the middle panel with swapped magnetization directions, i.e. the $DyFe_2$ layers parallel, the $ErFe_2$ layers antiparallel to the external field, and the bottom panel for the case of zero magnetization in both layers.

The reason for this element-specific magnetic information is the different nuclear SLD of $DyFe_2$ (Nb_{nuc} = 729 μm^{-2}) and $ErFe_2$ (Nb_{nuc} = 554 μm^{-2}). So, this type of element-specificity of PNR would not work for systems where the nuclear SLDs are identical or very close to each other.

CONCLUSION

The magnetization reversal experiments described here demonstrate the unique capabilities of Polarized Neutron Reflectometry for determining the magnetic structure of multilayers with different magnetic layers. PNR can determine complicated magnetic structures inaccessible to standard magnetometry techniques. PNR is capable of measuring element-specific hysteresis loops, *i.e.* PNR can distinguish the magnetization of different magnetic layers, where standard magnetometry techniques would only measure the average magnetization.

ACKNOWLEDGMENT

We are indebted to Zin Tun, CNBC, for his continuous efforts during the past decade to install and improve the neutron reflectometry set-up on C5 and for his time to explain to us how to use his set-up properly. We appreciate the careful reading of the manuscript by W.J.L. Buyers, Z. Tun, and M. Saoudi.

REFRENCES

1. A. Schreyer, J.F. Ankner, T. Zeidler, H. Zabel, M. Schäfer, J.A. Wolf, P. Grünberg, and C.F. Majkrzak, *Phys. Rev.* **B 52**, 16066 (1995).
2. A. Schreyer, C.F. Majkrzak, T. Zeidler, T. Schmitte, P. Bödeker, K. Theis-Bröhl, A. Abromeit, J.A. Dura, and T. Watanabe, *Phys. Rev. Lett.* **79**, 4914 (1997).
3. A. Schreyer, K. Bröhl, J.F. Ankner, C.F. Majkrzak, T. Zeidler, P. Bödeker, N. Metoki, and H. Zabel, *Phys. Rev.* **B 47**, 15334 (1993).
4. C. Rehm, D. Nagengast, F. Klose, H. Maletta, and A. Weidinger, *Europhys. Lett.* **38**, 61 (1997).
5. F. Klose, C. Rehm, D. Nagengast, H. Maletta, and A. Weidinger, *Phys. Rev. Lett.* **78**, 1150 (1997).
6. A. Schreyer, J.F. Ankner, M. Schäfer, T. Zeidler, H. Zabel, C.F. Majkrzak, and P. Grünberg, *J. Magn. Magn. Mater.* **148**, 189 (1995).
7. G.P. Felcher, W. Lohstroh, H. Fritzsche, M. Münzenberg, M. Maletta, and W. Felsch, *Appl. Phys. Lett.* **72**, 2894 (1998).
8. J.A.C. Bland, D. Pescia, and R.F. Willis, *Phys. Rev. Lett.* **58**, 1244 (1987).
9. T. Nawrath, H. Fritzsche, F. Klose, J. Nowikow, and H. Maletta, *Phys. Rev.* **B 60**, 9525 (1999).
10. H. Fritzsche, Y.T. Liu, J. Hauschild, and H. Maletta, *Phys. Rev.* **B 70**, 214406 (2004).
11. M.R. Fitzsimmons, P. Yashar, C. Leighton, I.K. Schuller, J. Nogués, C.F. Majkrzak, and J.A. Dura, *Phys. Rev. Lett.* **84**, 3986 (2000).
12. K. Temst, M.J. Van Bael, and H. Fritzsche, *Appl. Phys. Lett.* **79**, 991 (2001).
13. M. Pannetier, T.D. Doan, F. Ott, S. Berger, N. Persat, and C. Fermon, *Europhys. Lett.* **64**, 524 (2003).
14. M. Gierlings, M.J. Prandolini, H. Fritzsche, M. Gruyters, and D. Riegel, *Phys. Rev.* **B 65**, 92407 (2002).
15. W.T. Lee, S.G.E. te Velthuis, G.P. Felcher, F. Klose, T. Gredig, and E.D. Dahlberg, *Phys. Rev.* **B 65**, 224417 (2002).
16. F. Radu, M. Etzkorn, R. Siebrecht, T. Schmitte, K. Westerholt, and H. Zabel, *Phys. Rev.* **B 67**, 134409 (2003).
17. M. Gierlings, M.J. Prandolini, H. Fritzsche, M. Gruyters, and D. Riegel, *Physica* **B 356**, 36 (2005).
18. V.F. Sears, *Neutron News* **3**, 26 (1992).
19. www.ncnr.nist.gov/resources/n-lengths
20. L.G. Parratt, *Phys. Rev.* **95**, 359 (1954).
21. K. Temst, E. Kunnen, V.V. Moshchalkov, H. Maletta, H. Fritzsche, and Y. Bruynseraede, *Physica* **B** 276-278, 684 (2000).
22. G.P. Felcher, R.O. Hilleke, R.K. Crawford, J. Haumann, R. Kleb, and G. Ostrowski, *Rev. Sci. Instrum.* **58**, 609 (1987).
23. S.J. Blundell, and J.A.C. Bland, *Phys. Rev.* **B 46**, 3391 (1992).
24. F. Radu, V. Leiner, M. Wolff, V.K. Ignatovich, and H. Zabel, *Phys. Rev.* **B 71**, 214423 (2005).
25. J. Bergsma and C. van Dijk, *Nucl. Instr. and Meth.* **51**, 121 (1967).
26. F. Mezei, *Z. Physik* **255**, 146 (1972).
27. H. Fritzsche, *Rev. Sci. Instrum.* **76**, 115104 (2005).
28. U. Atzmony, and M.P. Dariel, *Phys. Rev.* **B 13**, 4006 (1976).
29. V. Oderno, C. Dufour, K. Dumesnil, P. Bauer, P. Mangin, and G. Marchal, *Phys. Rev.* **B 54**, R17375 (1996).
30. A. Mougin, C. Dufour, K. Dumesnil, and Ph. Mangin, *Phys. Rev.* **B 62**, 9517 (2000).
31. M.J. Bentall, R.A. Cowley, W.J.L. Buyers, Z. Tun, W. Lohstroh, R.C.C. Ward, and M.R. Wells, *J. Phys. Condens. Matter* **15**, 4301 (2003).